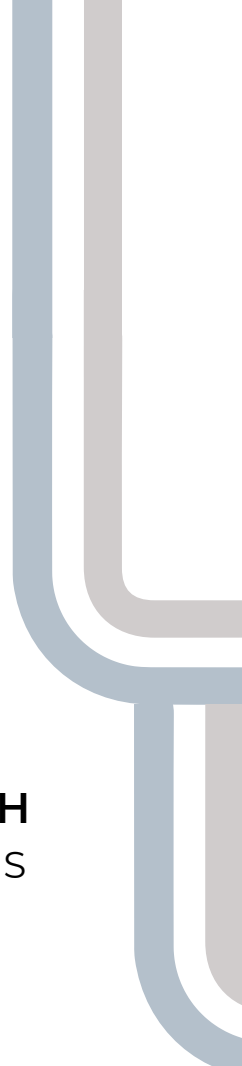




POLITECNICO
MILANO 1863

SCUOLA DI INGEGNERIA INDUSTRIALE
E DELL'INFORMAZIONE



ORBITAL MECHANICS

INTERPLANETARY MISSION FROM MERCURY TO EARTH

PLANETARY MISSION ON EARTH WITH LUNAR PERTURBATIONS

LAUREA MAGISTRALE
SPACE ENGINEERING

Prof Camilla Colombo

Presented by

Person code - Matriculation N.

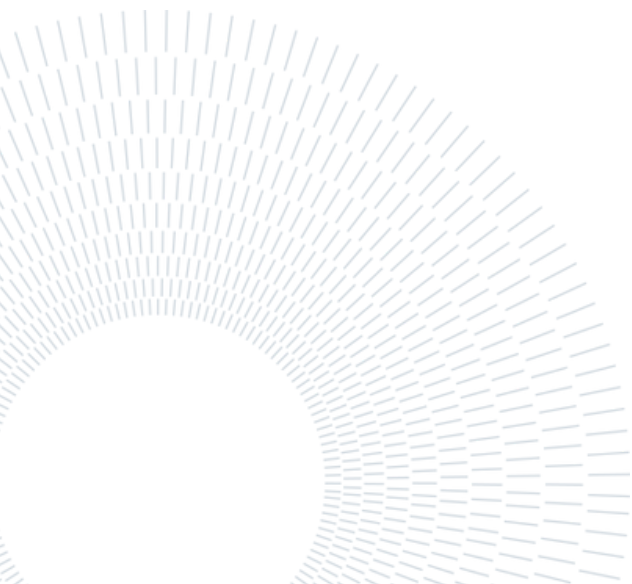
Azevedo Da Silva Esteban
11072547 - 277079

Domenichelli Eleonora
10797598 - 280323

Donati Filippo
10766052 - 280181

Pantoja Gavidia Maria Paulina
11021048 - 272281

Group 2427 Tzintzun
Academic year 2024/2025



1

Assignment 1: Interplanetary Mission

1.1. Introduction

This chapter discusses the design and analysis of an Interplanetary Explorer Mission that targets a near-Earth asteroid. The interplanetary trajectory involves departure from Mercury, a gravity-assist maneuver at Earth, and arrival at Asteroid No. 30. Complying with the assigned constraints, the earliest departure is set for January 1, 2030, and the latest arrival on January 1, 2060.

The feasibility analysis evaluates the mission's viability using the total cost in terms of Δv_{tot} as the primary figure of merit, constrained by the altitude during the flyby, limited to an approximate minimum of 2000 km before entering LEO orbits to avoid space debris. The patched conics method was employed to design the trajectory with the following assumptions:

- Planetary departure and insertion maneuvers were excluded from the analysis.
- The initial heliocentric orbit was assumed to match that of the departure planet, while the final heliocentric orbit was set to align with the arrival body's orbital parameters.
- All Δv maneuvers were treated as instantaneous events, neglecting burn duration.
- Solar radiation pressure, atmospheric drag, and other non-gravitational forces were disregarded to simplify the analysis.

1.2. Transfer windows and preliminary estimations

To determine an initial approximation of the mission's trajectory, the synodic periods of the planets and the asteroid were calculated using Equation 1.1 to identify potential launch windows based on the relative alignment of the celestial bodies. Among these, the Earth-asteroid synodic period was identified as the longest, approximately 1.3 years, providing a temporal constraint for the mission, due to that the transfer phase between Mercury and Earth must conclude within this period to align with the next favorable configuration for the Earth-asteroid transfer.

$$T_{synodic} = \frac{T_{\text{departure's planet}} * T_{\text{arrival's planet}}}{|T_{\text{departure's planet}} - T_{\text{arrival's planet}}|} \quad (1.1)$$

In addition to the synodic period analysis, Hohmann transfer times were calculated under the simplifying assumption of coplanar and circular orbits to identify potential launch windows within the constraints imposed by these periods, providing an approximation for estimating mission phases.

The Hohmann time of flight from Mercury to Earth was determined to be approximately 4 months, establishing the departure limit from Mercury within this duration to ensure compatibility with the Earth-asteroid synodic period, as shown in Figure 1.1. Similarly, the Hohmann transfer from Earth to the asteroid is estimated to take about 13 months, using this time frame to define the potential arrival dates at the asteroid based on its immediate transfer from Earth, also illustrated in Figure 1.1.

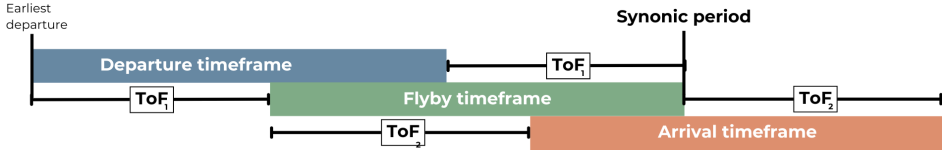


Figure 1.1: Initial time windows Overview

To establish the initial time windows, the previously described flight durations were adjusted by incorporating a 40% safety margin to account for potential perturbations that could affect the flight time when calculating the required velocities [1]. As a result, the initial time windows are defined as shown in Table 1.1.

Table 1.1: Initial time window's dates

Start date	End date	Start date	End date	Start date	End date
Departure Window Time		GA Window Time		Arrival Window Time	
Earliest dep. (E.D.) 01/01/2030	E.D. + (T_{syny} - ToF_1) 17/03/2031	E.D. + ToF_1 05/03/2030	Dep. end date + ToF_1 11/08/2031	Arr. start date + ToF_2 30/10/2030	Arr. end date + ToF_2 18/02/2033

1.3. Design Strategy

To determine the mission trajectory and identify the most efficient transfer windows, three optimization methods were evaluated within the defined initial window frame: Grid Search, Differential Evolution Algorithm, and Genetic Algorithm. These methods were applied to evaluate the Lambert transfer arc in each potential launch window, constrained by the condition that the arrival date must always occur after the gravity-assist date, which in turn must occur after the departure date (i.e., arrival date > gravity-assist date > departure date). During this evaluation, two Lambert interplanetary transfer arcs were established, connected by the powered gravity-assist maneuver performed during the flyby to bridge the two segments.

```

1  for t1 = w_dep
2      for t2 = w_fb
3          for t3 = w_arr
4              [ $\Delta_v$ ] = interplanetary(t1, t2, t3);

```

To implement the Grid Search method, the three degrees of freedom—departure date, flyby date, and arrival date—were discretized as the primary variables, as outlined below, with an initial step size of 1 day to ensure detailed sampling of the solution space; however, this approach resulted in a runtime of approximately 10,190 seconds, prompting an adjustment to a 10-day step size, which reduced computational time to 560 seconds, a 94.5% improvement.

The Differential Evolution Algorithm was implemented using Particle Swarm Optimization (PSO) to explore the solution space and identify optimal transfer trajectories, with a convergence analysis performed to evaluate the effect of the number of candidate solutions (particles) on the algorithm's performance. Figure 1.2a shows that convergence is reliably achieved when the swarm size reaches or exceeds 2000 particles, adopted to guarantee robust convergence while minimizing unnecessary computational overhead.

The Genetic Algorithm was employed defining an initial population of candidate solutions obtained by a convergence analysis, with Figure 1.2b showing that populations of at least 300 individuals

1|CHAPTER 1. ASSIGNMENT 1: INTERPLANETARY MISSION

ensured reliable convergence while maintaining computational efficiency.

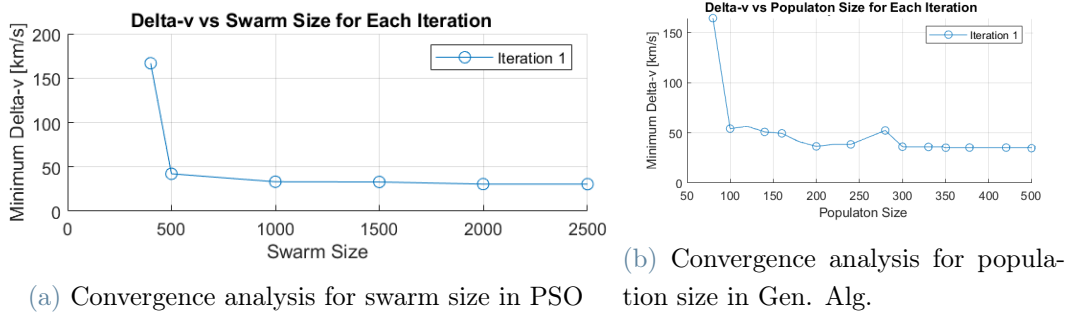


Figure 1.2: Convergence analysis for algorithms factors

To evaluate the performance of the three optimization methods, each algorithm was tested over three independent iterations to account for potential variability inherent to their statistical nature. As illustrated, in Figure 1.3 the Genetic Algorithm demonstrated consistent results achieving the lowest Δv values across all trials. As Genetic Algorithm offered the best balance between solution quality and computational cost, it was selected as the most suitable approach for this mission analysis.

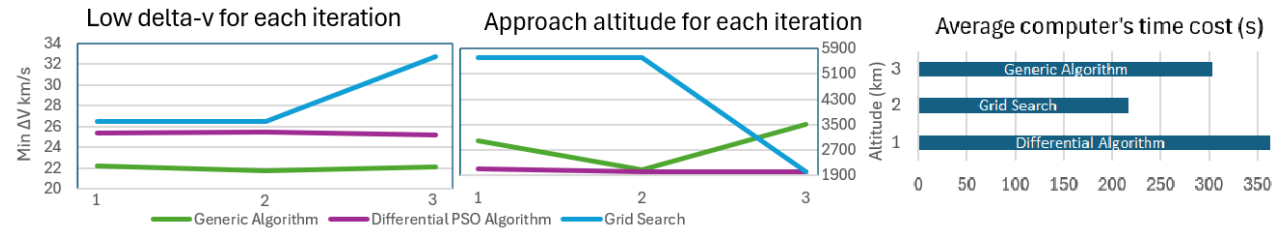


Figure 1.3: Algorithm's performance

To enhance the solutions provided by the Genetic Algorithm, three refinement methods—FMINCON, Gradient Refining Method (GRM), and Simulated Annealing (SAR)—were utilized, focusing on further reducing the total Δv and improving trajectory accuracy.

As summarized in Table 1.2, all three methods converged on similar trajectories, yielding comparable departure (t_1), flyby (t_2), and arrival (t_3) dates, along with the corresponding Δv . However, the inherent statistical variability of these methods and the Genetic Algorithm's outputs introduced slight variances across iterations, necessitating the implementation of a conditional selection mechanism that consistently identified the optimal solution.

Table 1.2: Results of refined methods

Method	t_1 mjd2000	t_2 mjd2000	t_3 mjd2000	Δv mjd2000
FMINCON	20898.9816	20945.9493	21267.7460	21.45
GRM	20898.9816	20945.9494	21267.7460	21.453147
SAR	20899.2032	20946.4608	21280.0645	21.33

1.4. Orbital characterization

The optimization algorithm and refinement methods described above were applied to evaluate potential solutions within a defined time window. Starting with the initial range proposed in Table 1.1, the algorithm iteratively shifted through subsequent windows of equal size over N-iterations until the best result was identified. Once the optimal solution was found, it was refined using the conditional selection mechanism to ensure the lowest total Δv , shown in Table 1.3 fully satisfying all mission constraints in the most suitable dates.

Table 1.3: Final dates selection

Departure date	G.A. date	Arrival date	Δv
21/03/2057	07/05/2057	06/04/2058	21.33 km/s

1.4.1. Transfer Window Visualization

In the porkchop plot shown in Figure 1.5, the Δv behavior of across various dates within the launch window is visualized detailing that for the Mercury-to-Earth transfer, the minimum Δv is located within a region of very low velocity requirements, confirming the optimality of its selection and ensuring proper alignment with the Earth flyby while minimizing the velocity demands for the first transfer arc.

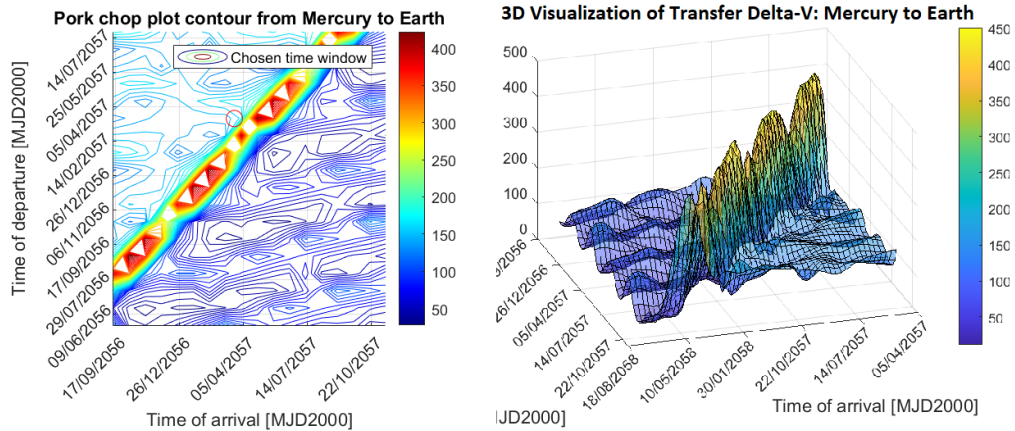


Figure 1.4: Porkchop plot contour from Mercury to Earth

Similarly, the Earth-to-Asteroid porkchop plot shows the chosen time window for the second transfer arc. As in the previous plot, the contour levels and color gradient highlight the Δv distribution, with the selected window positioned within the optimal region ensuring minimal velocity expenditure while adhering to the synodic constraints and the desired mission timeline.

1|CHAPTER 1. ASSIGNMENT 1: INTERPLANETARY MISSION

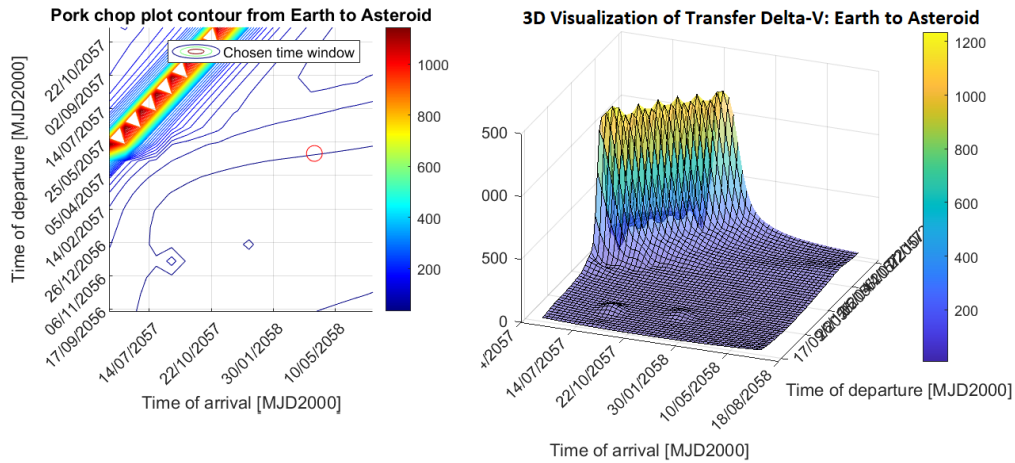


Figure 1.5: Porkchop plot contour from Earth to Asteroid no.30

1.4.2. Heliocentric Trajectory

The heliocentric trajectory was constructed based on the results obtained from the optimization process, which identified the minimum Δv and its corresponding dates. Using these results, two Lambert transfer arcs were solved: one connecting the departure from Mercury to the Earth flyby and another linking the Earth flyby to the asteroid. The initial conditions for these arcs were derived from the Keplerian elements of each celestial body, ensuring the accuracy of the transfer calculations. The characteristics of the transfer arcs are summarized in Table 1.4, and the trajectory is illustrated in Figure 1.6 (with Planets escalated as reference).

Table 1.4: Lambert's arcs characterization

	a (km)	e	i ($^{\circ}$)	Ω ($^{\circ}$)	ω ($^{\circ}$)	ϑ ($^{\circ}$)
Mer to Earth	172971938.00	0.72947	6.93	47.89	50.51	1.34
Earth to Ast.30	211833559.45	0.73215	0.30	47.89	61.53	28.31

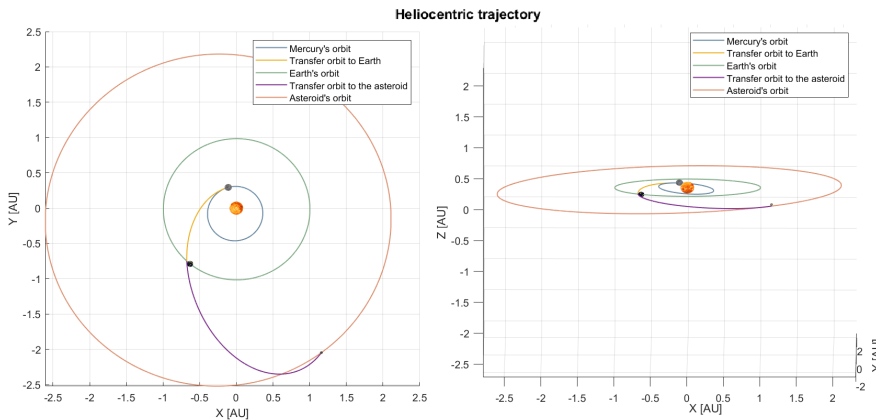


Figure 1.6: Heliocentric Trajectory

1|CHAPTER 1. ASSIGNMENT 1: INTERPLANETARY MISSION

1.4.3. Powered Gravity Assist Maneuver

To refine the trajectory and meet the mission requirements, a powered gravity assist was implemented at Earth, utilizing the planet's gravitational influence to modify the spacecraft's velocity vector. This maneuver was modeled within a finite sphere of influence (SOI) to optimize the subsequent transfer arc toward the asteroid, as depicted in Figure 1.7. The closest approach occurred at an altitude of approximately 3295.2 km, a value that effectively minimizes the cost of the maneuver at pericenter while ensuring a balance between reducing velocity expenditure and mitigating risks associated with entering low Earth orbit or encountering space debris.

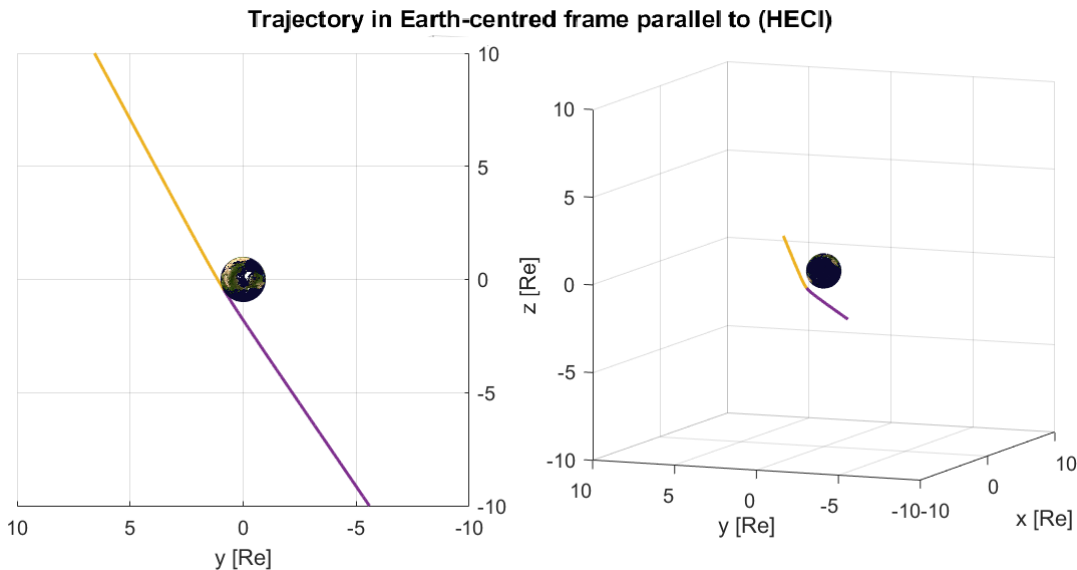


Figure 1.7: Flyby trajectory

The total Δv_{tot} budget for the mission is distributed across three phases: the departure maneuver (Δv_{dep}) from Mercury, the power gravity assist at Earth (Δv_{GA}) to connect the two Lambert transfer arcs, and the arrival maneuver (Δv_{arr}) at asteroid. Figure 1.8 summarizes the Δv distribution across the phases showing that flyby significantly reduced the overall cost by efficiently linking the two Lambert arcs and minimizing the energy required for the second transfer, this can be confirmed by comparing the velocity change during the flyby (Δv_{fb}) and the powered maneuver at pericenter (Δv_{gp}).

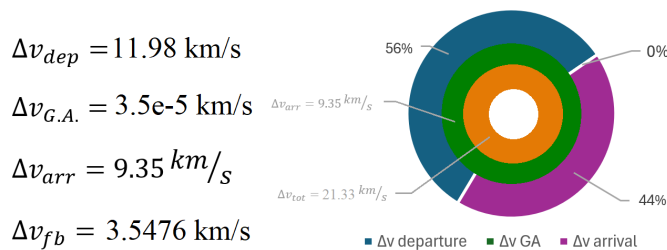


Figure 1.8: Cost distribution of delta-v

2

Assignment 2: Planetary Mission

2.1. Introduction

The second chapter aims to discuss the analysis of an orbit proposed for a Planetary Exploration Mission conducted around Earth. The propagation of the orbit and its ground track are studied, both considering and neglecting external perturbations. Orbit's parameters are then modified to achieve a repeating ground track. The analysis is performed for multiple relevant time intervals; two numerical propagation methods are employed and compared in terms of accuracy and computational efficiency.

2.2. Orbit characterization

The initial Keplerian parameters of the assigned Earth-centered orbit are listed in Table 2.1. Notice that Ω , ω , θ and the starting date of propagation were chosen freely.

Table 2.1: Initial Keplerian parameters

a [Km]	e [-]	i [deg]	Ω [deg]	ω [deg]	θ [deg]	T [s]	Date
23300	0.5230	58.65	0	0	0	35395	2057/05/08 23:20:30

The perturbing effects taken into account are:

- Earth's oblateness, expressed by the second zonal harmonic J2. The perturbing acceleration can be modeled as:

$$\underline{a}_{J_2} = \frac{3}{2} \frac{J_2 \mu R_e^2}{r^4} \left[\frac{x}{r} \left(5 \frac{z^2}{r^2} - 1 \right) \hat{i} + \frac{y}{r} \left(5 \frac{z^2}{r^2} - 1 \right) \hat{j} + \frac{z}{r} \left(5 \frac{z^2}{r^2} - 3 \right) \hat{k} \right] \quad (2.1)$$

where \hat{i} , \hat{j} , \hat{k} are the unit vectors of Geocentric Equatorial reference frame and x , y , z are the components of spacecraft's position vector \underline{r} .

- Gravitational influence of the Moon, that can be expressed as:

$$\underline{a}_{Moon} = \mu_M \left(\frac{\underline{r}_{SC/Moon}}{r_{SC/Moon}^3} - \frac{\underline{r}_{CB/Moon}}{r_{CB/Moon}^3} \right) \quad (2.2)$$

where $\underline{r}_{SC/Moon}$ is the position vector between S/C and the Moon and $\underline{r}_{CB/Moon}$ is the position vector between Earth and Moon.

2.3. Ground track

The ground track has been computed and plotted for three orbital periods ($T = 1$, $T = 13$, $T = 30$).

Due to Earth's rotation, the ground track experiences a westward shift of $\Delta\lambda = -T\omega_e = -147.8$ deg.

2|CHAPTER 2. ASSIGNMENT 2: PLANETARY MISSION

In the perturbed case, this shift is also affected by RAAN's precession primarily, although this effect is much smaller compared to Earth's rotation. As a result, the ground tracks of unperturbed and perturbed orbits remain similar over short time spans, with noticeable differences appearing only after significant time, as shown in last couple of pictures of Figure 2.1.

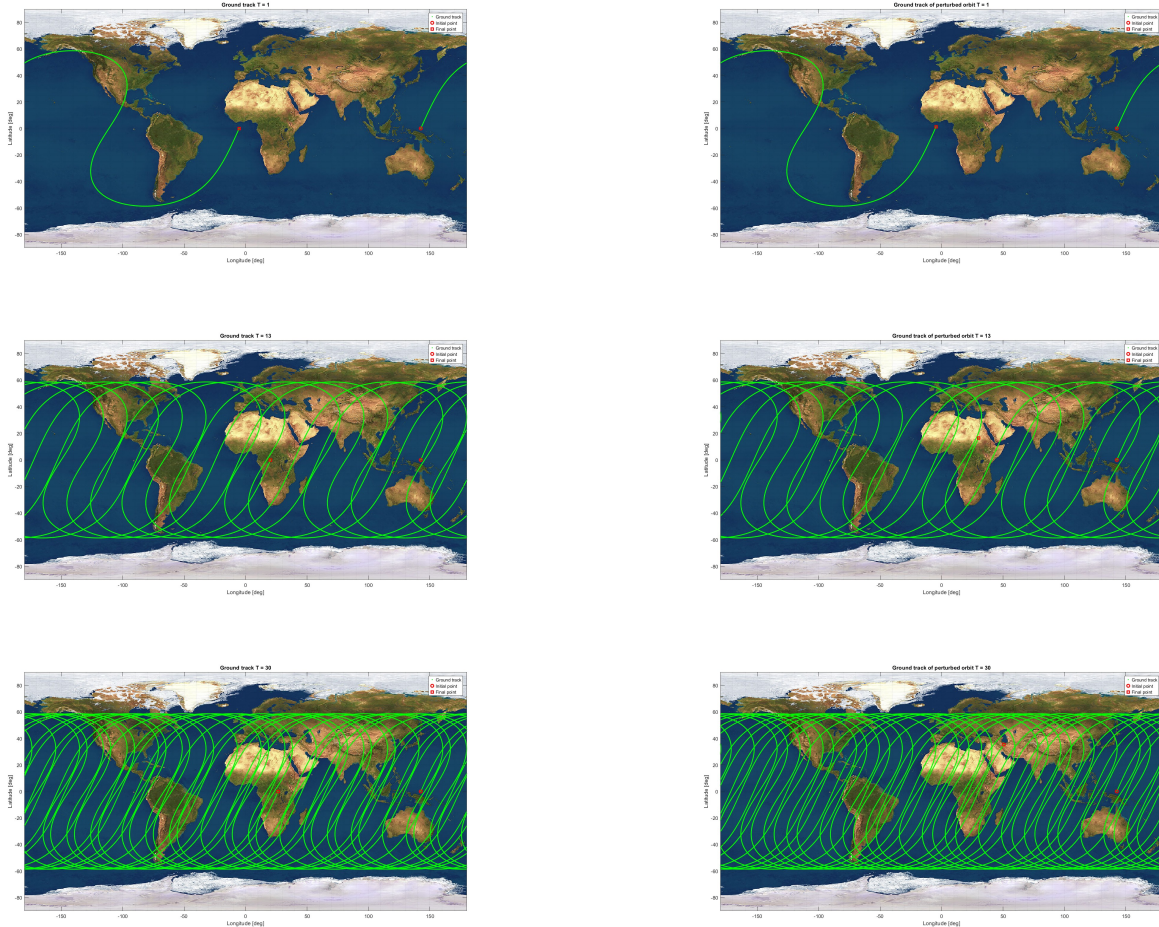


Figure 2.1: Unperturbed and perturbed ground track for T=1, T=13, T=30

2.3.1. Repeating ground track

In order to minimize the amount of ground stations required during the operational lifetime of the mission, the initial orbit was modified to achieve a repeating ground track after a set number of orbit revolutions k and Earth complete rotations m . For our specific mission it was required to guarantee that this phenomena happens after $k = 13$ and $m = 3$. To achieve this, the new value of the semi-major axis was designed using equation 2.3:

$$a_{rep} = \sqrt[3]{\frac{\mu}{(\omega_E \frac{k}{m})^2}} \quad (2.3)$$

This yields a modified semi-major axis of $a_{rep} = 15864$ km, that let the orbit remain inside the boundaries of the Earth sphere of influence. The new westward shift due to Earth's rotation is

2|CHAPTER 2. ASSIGNMENT 2: PLANETARY MISSION

$$\Delta\lambda_{rep} = -T_{rep}\omega_e = -83.07 \text{ deg.}$$

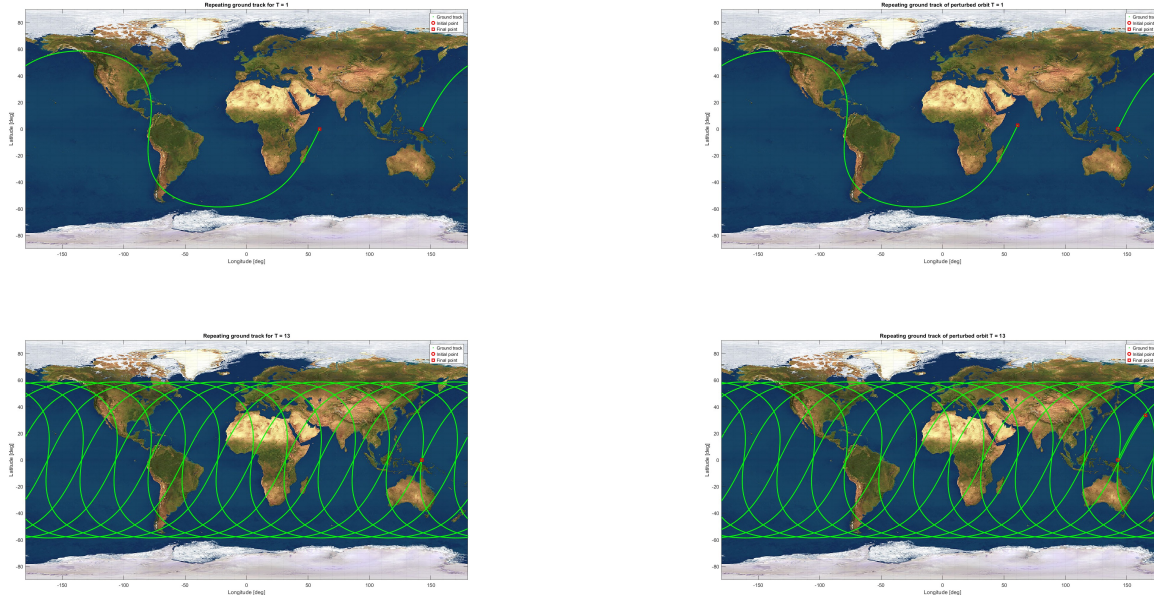


Figure 2.2: Unperturbed and perturbed repeating ground track for T=1 and T=13

The new semi-major axis is computed assuming an unperturbed situation, so the effect of perturbations becomes evident after one ground track repetition, as the initial and final points no longer coincide. A correction to the semi-major axis a_{rep} can be applied to restore the ground track repetition for the perturbed orbit

2.4. Orbit propagation

2.4.1. Propagation methods

Two orbit propagation methods were implemented:

- Cartesian coordinates propagation, integrating Kepler's equation and converting to orbital elements using *rv2parorb.m*;
- Keplerian elements propagation, directly integrating the derivatives of orbital elements from Gauss planetary equations, with perturbing acceleration expressed in the TNH (tangential-normal-out of plane) reference frame.

2.4.2. Evolution of Keplerian elements

Figure 2.3, 2.4, 2.5 illustrates the evolution of the Keplerian elements obtained using the two propagation methods. The first column presents the orbital elements derived from Cartesian coordinate propagation (labeled "Car" in the images captions), while the second column shows the parameters directly integrated using Gauss planetary equations (labeled "Kep"). The third column depicts the relative error between the two methods for each parameter. The computation spans 500 orbital revolutions, deemed sufficient to capture the most significant variations affecting the elements. A brief examination of the graphs reveals three distinct behaviours:

2|CHAPTER 2. ASSIGNMENT 2: PLANETARY MISSION

- Short-term oscillations of all orbital elements, caused by the orbit's dynamics;
- Long-term oscillations of e , i and ω , driven by the gravitational influence of the Moon;
- Secular effects on Ω and ω , resulting from Earth's oblateness.

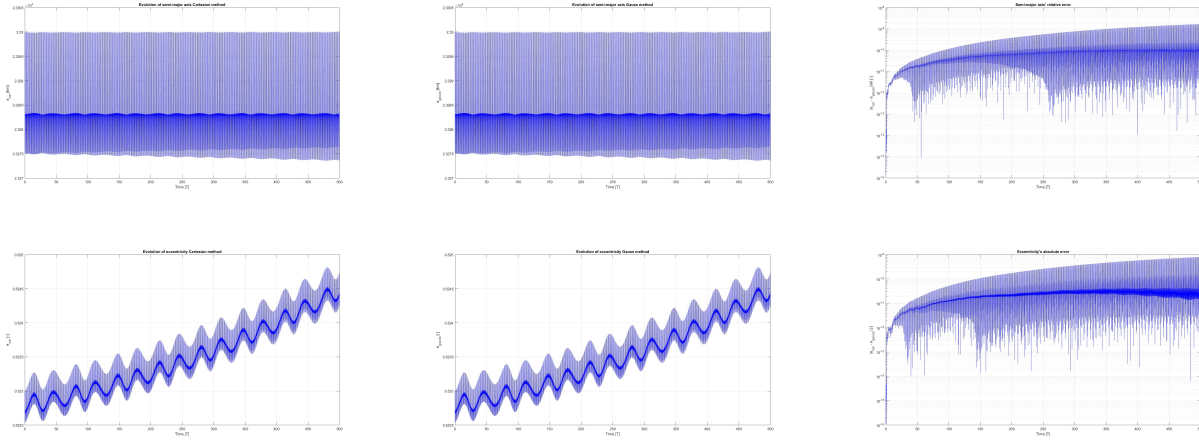


Figure 2.3: Evolution of a and e (Car and Kep respectively) and absolute and relative error between propagation methods.

The nodal regression and the perigee precession are both expected phenomena, as the influence of J2 on Ω and ω is well established; in particular, these variables exhibit a sinusoidal dependence on J2, and given the initial orbit's inclination ($63.4^\circ < i < 90^\circ$), it follows that $\dot{\Omega} < 0$ and $\dot{\omega} > 0$. These trends are immediately obvious from the graphs and could also be confirmed numerically. While secular contributions to the true anomaly are expected, these are harder to detect due to the unwrapped nature of the angle, which exhibits a linear component independent of the secular component of the variation in θ , so we won't discuss further this parameter.

The presence of the Moon affects mainly e and i , inducing long-term oscillations. While both parameters exhibit also a secular behavior, an increment of the propagation time reveals that this effect is just a very long-term oscillatory behavior caused by the third-body perturbation.

2|CHAPTER 2. ASSIGNMENT 2: PLANETARY MISSION

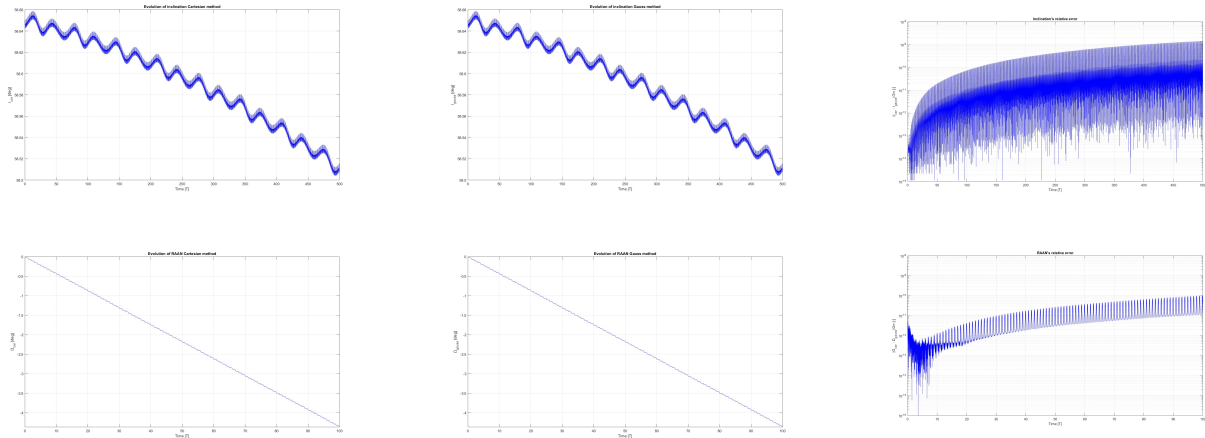


Figure 2.4: Evolution of i and Ω (Car and Kep respectively) and relative error between propagation methods.

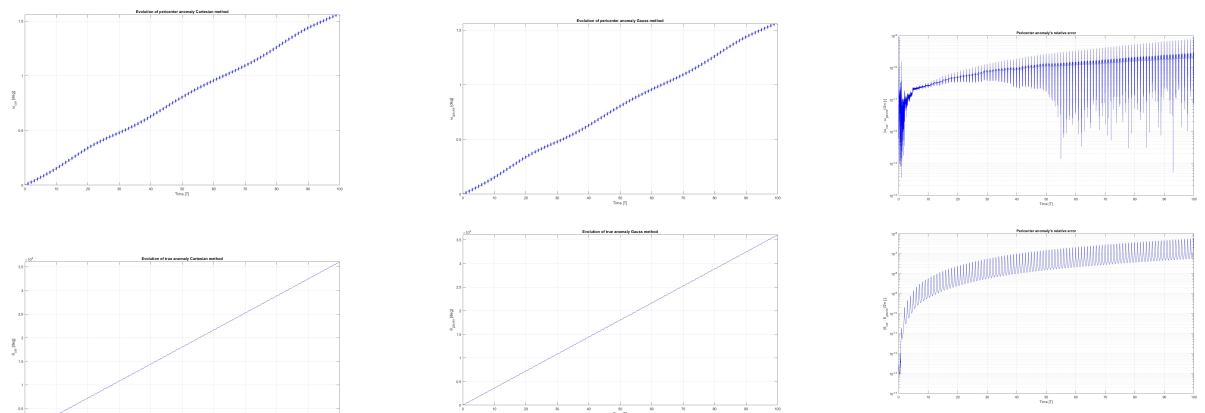
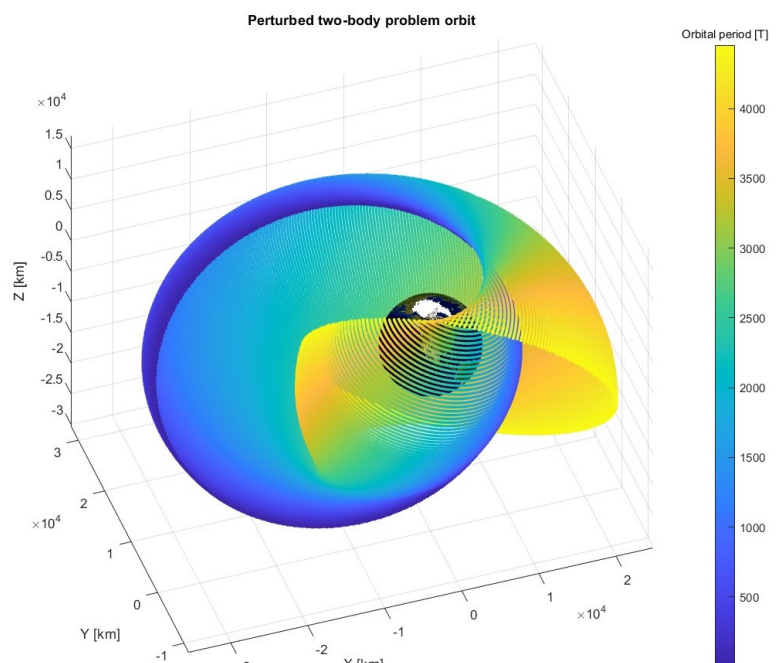


Figure 2.5: Evolution of ω and θ (Car and Kep respectively) and relative error between propagation methods.

At this point, the propagation time is furtherly extended to show the evolution of the orbit itself and fully appreciate the effect of perturbations on its shape and orientation at the same time. The initial Keplerian elements (2.1) were propagated for 4455 periods, which corresponds to approximately 5 years, and the results is shown in Figure 2.6:



2|CHAPTER 2. ASSIGNMENT 2: PLANETARY MISSION

2.4.3. Comparison

The graphs highlight that, in term of accuracy, once the tolerance for the ODE solver is set, the two methods show an almost equal behaviour. This can be also proven by computing the maximum absolute error between the propagated Keplerian elements.

Setting the *Relative tolerance* = $1e - 13$ and the *Absolute tolerance* = $1e - 14$ for the chosen ODE solver (*ode113*) and propagating for 500 orbits, the following results are obtained:

Table 2.2: Maximum Absolute Errors

$\ a \ _\infty [Km]$	$\ e \ _\infty [-]$	$\ i \ _\infty [\text{deg}]$	$\ \Omega \ _\infty [\text{deg}]$	$\ \omega \ _\infty [\text{deg}]$	$\ \theta \ _\infty [\text{deg}]$
$3.9986e^{-5}$	$8.1001e^{-10}$	$9.0042e^{-9}$	$2.2878e^{-8}$	$7.3266e^{-8}$	$6.7406e^{-5}$

In terms of computational efficiency, the simulations demonstrated a slightly better performance of Gauss method, which was as average 1 second faster than the other, when using 100,000 points for the time discretization.

2.5. Filtering

As already said, two main oscillatory behaviours have been noticed for the Keplerian elements: short periodic oscillations with a period of $1T$, and long periodic oscillations with a period of $15T$ (≈ 6 days). To recover long periodic and secular effects, the Keplerian elements were filtered using a low-pass filter, implemented through the MATLAB function *movmean.m*, with time windows, related to cut-off frequency, set equal to the two oscillatory periods.

Results are shown in Figure 2.7:

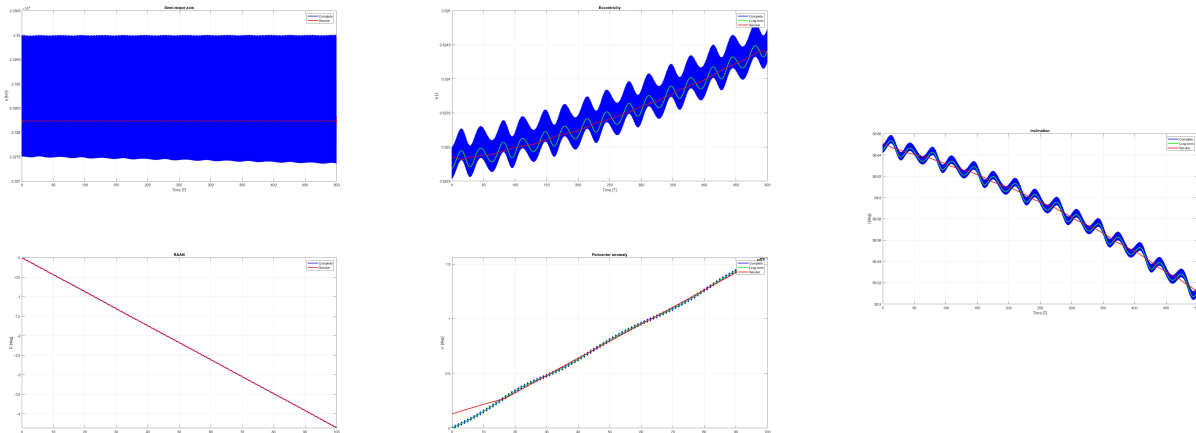


Figure 2.7: Keplerian element's filtering

2.6. Real data comparison

In this section we want to discuss the Keplerian elements evolution of two uncontrolled objects to see in real life the effects of orbit perturbations and compare it with the theory addressed during the lectures. Two suitable objects were found with the CelesTrack database and their ephemerides data were recovered from NASA/JPL's HORIZON propagator.

The first chosen object is a debris of IRIDIUM 33; which was a Russian communication satellite

2|CHAPTER 2. ASSIGNMENT 2: PLANETARY MISSION

located in LEO, with 779.6 km perigee altitude, 86.4° inclination and really low eccentricity. In 2009 it collided with Kosmos 2251, producing a large amount of space debris; the chosen debris has number 34102 in the NORAD catalog. The downloaded ephemerides cover the time span of 3 months, from April 1, 2024, to July 1, 2024.

From the graphs in Figure 2.9, it is possible to see that different perturbation effects are overlapping. It is immediate to notice a relevant variation on the semi-major axis, absent in the assigned case. This effect is given by the aerodynamic drag, that acts like a breaking velocity at the pericenter when the spacecraft is at lower altitudes, causing a decrease in the orbit energy, so a change of its shape, resulting in a decrease of both the semi-major axis and the eccentricity. However, the eccentricity's shape leads to believe in a more complex behavior. It is possible to immediately identify the secular effects associated to J2, nodal and perigee regression; everything is consistent with the theory, since the debris has an inclination of approximately 86.3 deg, that corresponds to $\dot{\Omega} < 0$ and $\dot{\omega} < 0$.

At $t = 3.5e6$, a noticeable discontinuity is observed in certain parameters, including the semi-major axis, the right ascension and the inclination. This anomaly could be attributed to a collision with another object or to a loss of mass.

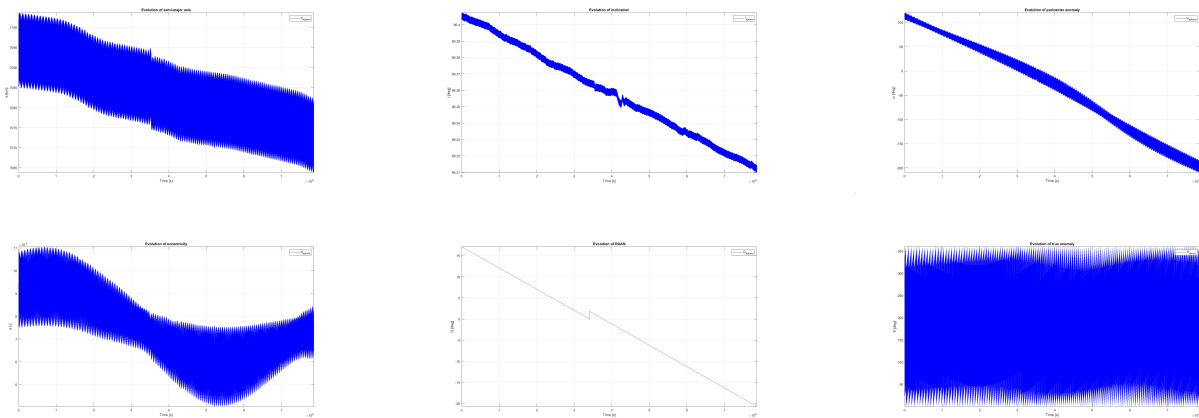


Figure 2.8: IRIDIUM 33 debris Keplerian elements evolution.

The second object chosen is OPS 5118, also known as Navstar 6; it was an American navigation satellite launched in 1980 as part of GPS, that was retired from service in 1991. It was located in a high MEO, with perigee altitude 20006 km, 62.8 deg inclination and low eccentricity. The ephemerides are retrieved for a six-months period, from April 1, 2024, to October 1, 2024.

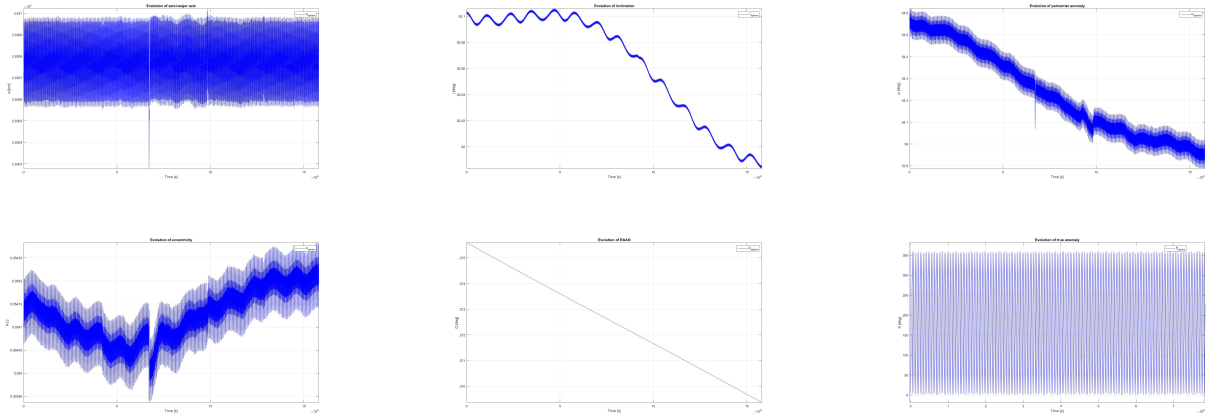


Figure 2.9: Navstar 6 Keplerian elements evolution.

It is possible to see that the global trending of the orbital parameters is pretty similar to the one of the assigned orbit (Figure 2.3, 2.4, 2.5). This confirms the prior analysis of the third body perturbation effects.

Comparing it to the previous debris, Ω and ω exhibit the same behavior of nodal and perigee regression associated to J2 effect, but on the perigee anomaly is possible to identify long-term oscillations, effect of the third body. Also the inclination and the eccentricity have both behaviors associated with solar and lunar gravity field perturbation. SRP's effect is not really evident in this short period of time since it is much smaller than other perturbations, even if the satellite has considerable dimensions. The semi-major axis value is constant as expected. Also in this case it is possible to observe a discontinuity in multiple orbital elements.

Bibliography

- [1] J. T. Olympio and C. H. Yam, “Deterministic method for space trajectory design with mission margin constraints,” in *61st International Astronautical Congress*, European Space Agency, ESTEC, The Netherlands, Prague, CZ, 2010.